Multiscale electrostatic analysis of silicon nanoelectromechanical systems (NEMS) via heterogeneous quantum models

Yang Xu and N. R. Aluru*
Beckman Institute for Advanced Science and Technology, University of Illinois at Urbana-Champaign, Urbana, Illinois 61801, USA
(Received 4 September 2007; published 11 February 2008)

A multiscale method, seamlessly combining semiclassical, effective-mass Schrödinger (EMS), and tight-binding (TB) theories, is proposed for electrostatic analysis of silicon nanoelectromechanical systems (NEMS). By using appropriate criteria, we identify the physical models that are accurate in each local region. If the local physical model is semiclassical, the charge density is directly computed by the semiclassical theory. If the local physical model is quantum mechanical (the EMS or TB model), the charge density is calculated by using the theory of local density of states (LDOS). The LDOS is efficiently calculated from the Green's function by using Haydock's recursion method where the Green's function is expressed as a continued fraction based on the local Hamiltonian. Once the charge density is determined, a Poisson equation is solved self-consistently to determine the electronic properties. The accuracy and efficiency of the multiscale method are demonstrated by considering two NEMS examples, namely, a silicon fixed-fixed beam with hydrogen termination surfaces and another silicon beam switch with 90° single period partial dislocations. The accuracy and efficiency of the multiscale method are demonstrated.

DOI: 10.1103/PhysRevB.77.075313 PACS number(s): 85.85.+j, 47.11.St, 41.20.Cv

I. INTRODUCTION

As significant progress is being made in various fields of nanotechnology, predicting electronic and mechanical properties of semiconductor devices is a compelling challenge from both the scientific and engineering viewpoints. In complex physical systems, the length scales can vary from a few nanometers to several hundreds of microns and predicting the physical properties at all length scales accurately and efficiently is a significant computational challenge. Multiscale computational methods aim to couple different length scales into one single framework.[1–7] Several multiscale methods have been proposed in the literature to solve complex problems in solid and fluid mechanics. For example, the concurrent handshaking multiscale method has been shown to successfully simulate crack propagation in silicon nanostructures;[1] heterogeneous multiscale methods, which use molecular dynamics at the microscale and continuum mechanics at the macroscale, have been used to compute the mechanical properties of various silicon structures.[2,7] In contrast, there has been comparatively little effort devoted to multiple scale analysis of electrostatics, which is an important energy domain for the analysis of nanoelectromechanical systems (NEMS). In this paper, we propose a multiscale method for the electrostatic analysis of silicon nanoelectromechanical systems.

Realistic silicon NEMS structures contain bulklike subdomains, quantum confinement regions, and defect areas. Typically, bulklike subdomains can be accurately modeled by a semiclassical theory, quantum confinement regions can be accurately modeled by an effective-mass Schrödinger (EMS) theory, and defect areas can be modeled by tight-binding (TB) methods. The use of any one of these physical theories to model the entire NEM structure can either be inaccurate or computationally infeasible. As a result, development of a multiscale method that can seamlessly combine various physical theories is critical for the accurate and efficient electrostatic analysis of NEMS. Our proposed multiscale scheme is conceptually illustrated in Fig. 1. We deal with two-dimensional electrostatic problems in this paper, but the approach can be easily extended to three-dimensional problems. The semiconductor device is first discretized into points—these points are referred to as the Poisson points. At each point, by using appropriate criteria, which will be discussed in detail later, we determine if the local region surrounding the point can be treated by the semiclassical, EMS, or TB model. When the quantum-mechanical models (the

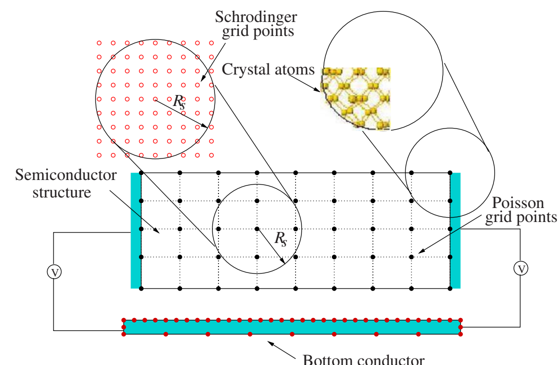

FIG. 1. (Color online) Illustration of the multiscale approach for a typical NEMS example consisting a semiconductor beam structure and a bottom conductor. The semiconductor beam region is discretized into Poisson grid points. The filled circles represent the Poisson grid points. In the region where the quantum effects are important, a sampling region (typically circular, but other shapes can also be easily considered) is required to compute LDOS at the Poisson point. The radius of the sampling region is denoted by R_S. The open circles in the EMS sampling regions represent the Schrödinger grid points. The atomic structure in the TB sampling regions represents the TB atom sites. The LDOS in the EMS and TB regions are calculated from the EMS and the TB Hamiltonian, respectively.

 ©2008 The American Physical Society

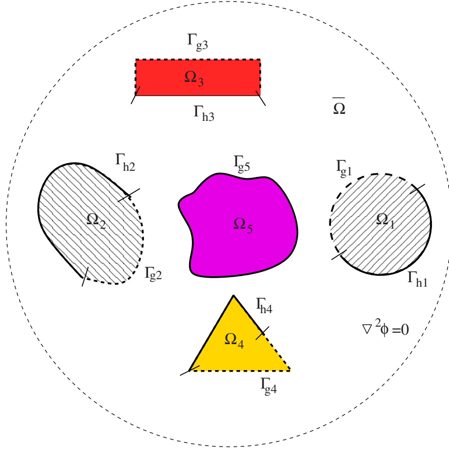

FIG. 2. (Color online) The electrostatic semiconductor system.

EMS or TB model) are required, one cannot solve the EMS or TB equation in a local region by direct domain decomposition to determine the charge distribution, as the boundary conditions on the wave functions are not known on the boundaries of the local region. Instead, in our multiscale model, the charge density is obtained from the local density of states (LDOS).[8] To compute the LDOS, only a finite-size sampling region (shown as a circular disk of radius R_S in Fig. 1) centered at the Poisson grid point is required by applying Kohn's "nearsightedness" principle.[13,14] As shown in Fig. 1, if the sampling region intersects the physical boundaries of the semiconductor, then the sampling region is appropriately modified. The EMS sampling region is composed of Schrödinger grid points and the TB sampling region is composed of the real atomistic structure. The LDOS is computed from the Green's function of the Hamiltonian matrix by using a recursion method.[15] As the number of recursion levels computed is usually far less than the dimension of the Hamiltonian matrix, the recursion method is an efficient approach to compute the LDOS and other electronic properties.

The multiscale method described above seamlessly combines the semiclassical and heterogeneous quantum-mechanical models. Quantum-mechanical effects are included only in the regions where they are necessary. As a result, semiconductor nanostructures which can be described entirely by semiclassical or quantum models or by combined semiclassical and quantum models are accurately modeled. The rest of the paper is organized as follows. Section II describes the theory and implementation of the proposed multiscale model. Section III presents results for several examples demonstrating the accuracy and efficiency of the multiscale method and conclusions are given in Sec. IV.

II. THEORY

A. Physical models

To illustrate the multiscale approach for electrostatic analysis of semiconductor nanostructures, we consider a general semiconductor system shown in Fig. 2. We deal with two-dimensional (2D) electrostatic problems in this paper, but the approach can be easily extended to three-dimensional problems. Consider a system of objects including semiconductors $(\Omega_1,\Omega_2,\ldots,\Omega_{N_0})$, where N_0 is the number of objects, embedded in a uniform dielectric medium $\bar{\Omega}$, as shown in Fig. 2. Potential $\phi(\mathbf{x})$ and its normal derivative $q(\mathbf{x})$ are given by $g_\gamma(\mathbf{x})$ and $h_\gamma(\mathbf{x})$ on portions of the boundary of each semiconductor, $\Gamma_{g\gamma}$ and $\Gamma_{h\gamma}$, $\gamma=1,2,\ldots,N_0$, respectively, where $\mathbf{x}=(x,y)^T$ is the position vector of any point. The governing equations for electrostatic analysis along with the boundary conditions are given by[8]

$$\nabla\cdot[\epsilon_s\nabla\phi(\mathbf{x})]=-\rho(\mathbf{x})=-e[p(\mathbf{x})-n(\mathbf{x})+N_D^+(\mathbf{x})-N_A^-(\mathbf{x})]\quad\text{in }\Omega_\gamma,\quad\gamma=1,\ldots,N_0,\tag{1}$$

$$\nabla^2\phi(\mathbf{x})=0\quad\text{in }\bar{\Omega},\tag{2}$$

$$\phi(\mathbf{x})=g_\gamma(\mathbf{x})\quad\text{on }\Gamma_{g\gamma},\quad\gamma=1,\ldots,N_0,\tag{3}$$

$$q(\mathbf{x})=\frac{\partial\phi(\mathbf{x})}{\partial\mathbf{n}}=h_\gamma(\mathbf{x})\quad\text{on }\Gamma_{h\gamma},\quad\gamma=1,\ldots,N_0,\tag{4}$$

where $\rho(\mathbf{x})$ is the charge density, $p(\mathbf{x})$ and $n(\mathbf{x})$ are hole and electron densities, respectively, $N_D^+(\mathbf{x})$ and $N_A^-(\mathbf{x})$ are the ionized donor and acceptor concentrations, respectively, ϵ_s is the permittivity of the semiconductor material, and e is the elementary charge.

In the exterior domain $\bar{\Omega}$, the Laplace equation is satisfied, as shown in Eq. (2). Note that the exterior domain $\bar{\Omega}$ is an open domain. A boundary integral equation (BIE) of the 2D Laplace equation is used to treat the exterior electrostatic problem,[9] i.e.,

$$\alpha(\mathbf{x})\phi(\mathbf{x})=\sum_{\gamma=1}^{N_0}\int_{\Gamma_\gamma}\phi(\mathbf{x}')\frac{\partial G(\mathbf{x},\mathbf{x}')}{\partial\mathbf{n}'}d\Gamma_\gamma(\mathbf{x}')-\sum_{\gamma=1}^{N_0}\int_{\Gamma_\gamma}\frac{\partial\phi(\mathbf{x}')}{\partial\mathbf{n}'}G(\mathbf{x},\mathbf{x}')d\Gamma_\gamma(\mathbf{x}')+\phi_\infty,\tag{5}$$

$$\sum_{\gamma=1}^{N_0}\int_{\Gamma_\gamma}\frac{\partial\phi(\mathbf{x}')}{\partial\mathbf{n}'}d\Gamma_\gamma(\mathbf{x}')=0,\tag{6}$$

where α is the corner tensor ($\alpha=1/2$ for smooth boundaries, see Ref. 10 for details) and $G(\mathbf{x},\mathbf{x}')=\frac{1}{2\pi}\ln|\mathbf{x}-\mathbf{x}'|$ is the Green's function. In 2D problems, the potential at infinity is the reference potential, ϕ_∞. The boundary integral equations [Eqs. (5) and (6)] are coupled with the Poisson equation [Eq. (1)] through the interface conditions given by[11]

$$\phi(\mathbf{x})|_{\text{BIE}}=\phi(\mathbf{x})|_{\text{Poisson}}\quad\text{on }\Gamma_{g\gamma},\quad\gamma=1,2,\ldots,N_0,\tag{7}$$

$$\epsilon_s\left.\frac{\partial\phi(\mathbf{x})}{\partial\mathbf{n}}\right|_{\text{Poisson}}+\epsilon_d\left.\frac{\partial\phi(\mathbf{x})}{\partial\mathbf{n}}\right|_{\text{BIE}}=\sigma_{\text{int}}\quad\text{on }\Gamma_{h\gamma},$$

$$\gamma = 1,2, \ldots ,N_0, \tag{8}$$

where $\phi(\mathbf{x})|_{\text{BIE}}$ and $\phi(\mathbf{x})|_{\text{Poisson}}$ are the potentials from the boundary integral equation and Poisson equation, respectively, $\frac{\partial\phi(\mathbf{x})}{\partial\mathbf{n}}|_{\text{BIE}}$ and $\frac{\partial\phi(\mathbf{x})}{\partial\mathbf{n}}|_{\text{Poisson}}$ are the normal derivatives of the potential from the boundary integral equation and Poisson equation, respectively, ϵ_d is the permittivity of the dielectric medium, and σ_{int} is the charge density on the exposed surface of the semiconductor. In this paper, for the purpose of illustrating the multiscale approach, the charge density on the surface is assumed to be zero. However, nonzero interface charge density σ_{int} can also be implemented easily. The potential $\phi(\mathbf{x})$ and the charge density $\rho(\mathbf{x})$ are obtained by solving Eqs. (1)–(8) self-consistently. In this paper, the interior Poisson's equation [Eq. (1)] is solved by using the finite difference method[12] and the boundary integral equations [Eqs. (5) and (6)] are solved by the boundary element method.[10]

In the multiscale approach, the choice of a physical model for a particular region is closely related to the accuracy and efficiency of the physical model for that particular region. There are a number of physical models for electrostatic analysis such as the classical Laplace conductor model, semiclassical Poisson model, effective potential model, EMS model, TB model, density functional theory model, etc.[8,16] Here, we only discuss three of these physical models, one for each scale, namely, the semiclassical Poisson model for microscale, the EMS model for nanoscale, and the TB model for atomistic scale.

1. Semiclassical model: Semiclassical Poisson equation

When the geometrical characteristic length of the device is comparable to the Debye screening length,[17] the semiclassical model is necessary to compute the charge density distribution. In the semiclassical model, the electron and hole density in the Poisson equation can be obtained as[8]

$$n(\mathbf{x}) = N_C \frac{2}{\sqrt{\pi}} \mathcal{F}_{1/2}\left[\frac{E_F - E_C(\mathbf{x})}{k_B T}\right], \tag{9}$$

$$p(\mathbf{x}) = N_V \frac{2}{\sqrt{\pi}} \mathcal{F}_{1/2}\left[\frac{E_V(\mathbf{x}) - E_F}{k_B T}\right], \tag{10}$$

where N_C and N_V are the effective density of states of conduction and valence bands, respectively, $\mathcal{F}_{1/2}$ is the complete Fermi-Dirac integral of order 1/2, $E_C(\mathbf{x})$ is the conduction band energy given by $E_C(\mathbf{x}) = -e\phi(\mathbf{x}) + \frac{E_g}{2}$, where E_g is the energy gap, e is the elementary charge, $E_V(\mathbf{x})$ is the valence band energy given by $E_V(\mathbf{x}) = -e\phi(\mathbf{x}) - \frac{E_g}{2}$, E_F is the Fermi energy, k_B is the Boltzmann constant, and T is the temperature, which is set to be the room temperature in this work. The main advantage of the semiclassical model is its simplicity, but the model can suffer from inaccuracies when quantum effects are important.

2. Quantum-mechanical model: Effective-mass Schrödinger equation

When the critical size of the device approaches the nanometer scale, quantum effects such as the carrier quantum confinement in the semiconductor structure become significant.[17] The quantum effects in the device can be accounted for by solving the EMS equation in the entire semiconductor domain. The EMS equation is given by

$$\begin{aligned} H\psi_n(\mathbf{r}) &= -\left[\frac{\hbar^2}{2}\frac{\partial}{\partial x}\left(\frac{1}{m_x^*}\frac{\partial}{\partial x}\right) + \frac{\hbar^2}{2}\frac{\partial}{\partial y}\left(\frac{1}{m_y^*}\frac{\partial}{\partial y}\right)\right]\psi_n(\mathbf{r}) \\ &\quad + e\phi(\mathbf{r})\psi_n(\mathbf{r}) \\ &= E_n\psi_n(\mathbf{r}), \end{aligned} \tag{11}$$

where H is the system Hamiltonian based on the effective-mass approximation, $\hbar$ is the reduced Planck's constant, m_x^* and m_y^* are the effective masses along the x and y axes, respectively, $\mathbf{r} = (x,y)^T$ is the position vector of any Schrödinger point, $\psi_n(\mathbf{r})$ is the nth eigen-wave-function, and E_n is the nth eigenvalue of the Hamiltonian H. If m_x^* and m_y^* are electron masses, then the Hamiltonian, $\psi_n(\mathbf{r})$, and E_n are computed for electrons. If m_x^* and m_y^* are hole masses, then the Hamiltonian, $\psi_n(\mathbf{r})$, and E_n are for holes. If we discretize the domain into N_S Schrödinger grid points and the grid spacings along the x axis and the y axis are denoted by Δx_S and Δy_S, respectively, then using the finite difference method, the EMS Hamiltonian elements in Eq. (11) can be rewritten as

$$H_{i,j} = \begin{cases} \left[\frac{\hbar^2}{m_x^*}\frac{1}{\Delta x_S^2} + \frac{\hbar^2}{m_y^*}\frac{1}{\Delta y_S^2} + e\phi(r_i)\right] & \text{when } i = j \\ -\frac{\hbar^2}{2m_x^*}\frac{1}{\Delta x_S^2} & \text{when points } i \text{ and } j \text{ are neighbors along the } x \text{ axis,} \\ -\frac{\hbar^2}{2m_y^*}\frac{1}{\Delta y_S^2} & \text{when points } i \text{ and } j \text{ are neighbors along the } y \text{ axis} \\ 0 & \text{otherwise,} \end{cases} \tag{12}$$

where $i, j = 1, \ldots, N_S$.

Once the Hamiltonian elements are obtained through Eq. (12), we can solve the EMS equation [Eq. (11)] numerically. After solving the eigensystem, all the eigenenergies and eigen wavefunctions are known. Then, the electron density $n(\mathbf{r})$ and hole density $p(\mathbf{r})$ can be computed by

$$n(\mathbf{r}) = N_n \sum_n |\psi_n(\mathbf{r})|^2 \mathcal{F}_{-1/2}\left(\frac{E_F - E_n}{k_B T}\right), \qquad (13)$$

$$p(\mathbf{r}) = N_p \sum_n |\psi_n(\mathbf{r})|^2 \mathcal{F}_{-1/2}\left(\frac{E_n - E_F}{k_B T}\right), \qquad (14)$$

where the coefficients N_n and N_p are

$$N_n = g_n \frac{1}{\pi}\left(\frac{2m_n^* k_B T}{\hbar^2}\right)^{1/2}, \qquad (15)$$

$$N_p = g_p \frac{1}{\pi}\left(\frac{2m_p^* k_B T}{\hbar^2}\right)^{1/2}, \qquad (16)$$

for the conduction band and valence band, respectively, $\mathcal{F}_{-1/2}$ is the complete Fermi-Dirac integral of order $-1/2$, constants g_n and g_p are the semiconductor conduction band degeneracy and valence band degeneracy, respectively, m_n^* and m_p^* are the density of state masses of electrons and holes, respectively, and the summations in Eqs. (13) and (14) are over all the energy levels. Note that the solution of the EMS equation [Eq. (11)] requires an eigensolution in the entire semiconductor domain. This can be expensive and inefficient when simulating large devices.

3. Quantum-mechanical model: Tight-binding approach

The EMS approach can be inaccurate when the critical size of nanostructures is within a few nanometers or when defects and other material inhomogeneities in nanostructures become important. To overcome the limitations of the EMS approach, more accurate quantum-mechanical models are required. *Ab initio* methods are typically accurate to predict electronic properties of nanostructures. However, the high computational cost prevents their widespread use. An alternative is to use TB methods, which are somewhat less accurate but computationally more efficient compared to *ab initio* methods. In this paper, we choose a nearest neighbor $sp^3d^5s^*$ orthogonal TB approach[18] as the atomistic quantum-mechanical model for defects and surface states.

In the TB scheme, the electronic wave functions $\psi_n(\mathbf{r})$ are expressed as a linear combination of atomic orbitals, $\psi_n(\mathbf{r}) = \Sigma_{i\alpha} c_{i\alpha}^{(n)} \varphi_{i\alpha}(\mathbf{r})$, where $\varphi_{i\alpha}(\mathbf{r})$ is the αth atomic orbital wave function at site i and $c_{i\alpha}^{(n)}$ is the nth coefficient. The TB Hamiltonian is defined in terms of parametrized matrix elements.[19–21] These parametrized matrix elements are usually constructed by fitting to experimental and/or first-principles database of properties of both bulk systems and clusters. The diagonal elements of the Hamiltonian matrix $\epsilon_{i\alpha}$ represent the on-site energies of atomic orbitals. The atomic orbital α, for example, for the $sp^3d^5s^*$ TB model used in this paper, can represent any of s, p_x, p_y, p_z, d_{xy}, d_{yz}, d_{zx}, $d_{x^2-y^2}$, $d_{3z^2-r^2}$, or s^* orbitals.[18,19] The intersite elements $H^0_{i\alpha,j\beta}$ describe the bond energies between the αth orbital of atom i and the βth orbital of atom j, and these are determined by using the tables of Slater and Koster.[19] For example, H^0_{is,jp_x} is given by

TABLE I. TB parameters for silicon and hydrogen (Refs. 18 and 25).

Parameter	Si-Si interaction	Si-H interaction
$\eta_{ss\sigma}$ (eV)	−1.95933	−3.99972
$\eta_{ss^*\sigma}$ (eV)	−1.52230	−1.69770
$\eta_{sp\sigma}$ (eV)	3.02562	4.25175
$\eta_{sd\sigma}$ (eV)	−2.28485	−2.10552
$\eta_{s^*s^*\sigma}$ (eV)	−4.24135	
$\eta_{s^*p\sigma}$ (eV)	3.15565	
$\eta_{s^*d\sigma}$ (eV)	−0.80993	
$\eta_{pp\sigma}$ (eV)	4.10364	
$\eta_{pp\pi}$ (eV)	−1.51801	
$\eta_{pd\sigma}$ (eV)	−1.35554	
$\eta_{pd\pi}$ (eV)	2.38479	
$\eta_{dd\sigma}$ (eV)	−1.68136	
$\eta_{dd\pi}$ (eV)	2.58880	
$\eta_{dd\delta}$ (eV)	−1.81400	
d_0 (Å)	2.352	1.478
	Si	H
ϵ_s (eV)	−2.15168	0.99984
ϵ_p (eV)	4.22925	
ϵ_{s^*} (eV)	19.11650	
ϵ_d (eV)	13.78950	
Z_c(e)	4.0	1.0

$$H^0_{is,jp_x} = l_x V_{sp\sigma}(r_{ij}), \qquad (17)$$

where $r_{ij} = |\mathbf{R}_j - \mathbf{R}_i|$ is the distance between atoms i and j, $\mathbf{R}_i = \{x_i y_i z_i\}^T$ and $\mathbf{R}_j = \{x_j y_j z_j\}^T$ are the position vectors of atoms i and j, respectively, l_x denotes the x direction cosine of the vector $(\mathbf{R}_j - \mathbf{R}_i)$, and $V_{sp\sigma}(r_{ij})$ is the element corresponding to the hopping bond energy of forming σ bond between the s orbital of atom i and the p orbital of atom j.[19–21] In this paper, these elements are taken to follow Harrison's rule,[21–24] i.e.,

$$V_{sp\sigma}(r_{ij}) = \eta_{sp\sigma} \frac{\hbar^2}{m_0 r_{ij}^2}, \qquad (18)$$

where m_0 is the electron mass and $\eta_{sp\sigma}$ is one of the TB hopping parameters. The TB parameters we use have been optimized by Boykin *et al.*[18] and Zheng *et al.*[25] to accurately reproduce the band gap and effective masses of bulk Si. All the silicon hopping parameters and on-site-energy parameters of the $sp^3d^5s^*$ TB model are listed in Table I.[18] When simulating the nanostructure surfaces, the silicon surface atoms with dangling bonds are passivated with hydrogen atoms in this paper. The TB parameters for hydrogen atoms, adopted from Zheng *et al.*,[25] are also listed in Table I. The TB Hamiltonian elements can be written in a general form given by

$$H_{i\alpha,j\beta}=\begin{cases}[\epsilon_{i\alpha}+e\phi(r_i)] & \text{when } i=j \text{ and } \alpha=\beta\\ H^0_{\alpha\beta}(r_{ij}) & \text{when atoms } i \text{ and } j \text{ are nearest neighbors}\\ 0 & \text{otherwise,}\end{cases} \tag{19}$$

where $H^0_{\alpha\beta}(r_{ij})$ are directly obtained from the Slater and Koster's table.[19]

Once the Hamiltonian is obtained, the electronic wave functions and eigenenergies of the tight-binding system are computed by solving the characteristic equation[26,27]

$$HC^{(n)}=E_nC^{(n)}, \tag{20}$$

where E_n is the nth eigenenergy of the system and $C^{(n)}$ is the column vector comprising the $c_{i\alpha}$ coefficients. After the wave functions are known, the atomic electron charges can be computed by

$$n_e(\mathbf{r})=2\sum_{n,i\alpha}\frac{|c^{(n)}_{i\alpha}\varphi_{i\alpha}(\mathbf{r})|^2}{e^{(E_n-E_f)/KT}+1}. \tag{21}$$

In a self-consistent approach, the electrostatic potential contribution to the on-site terms of the TB Hamiltonian $\phi(r_i)$ is updated by solving the Poisson equation. An initial guess of the potential is required to compute the total Hamiltonian H. In this paper, we use the semiclassical potential distribution as the initial guess. After the total Hamiltonian is computed, Eq. (20) is solved to obtain the eigenenergies and the wave functions of the system. The wave functions are then used to compute the charge density by using Eq. (21). Next, the Poisson equation is solved to update the potential distribution. This process is repeated until the self-consistent solution is obtained. Note that the direct solution of the TB equation [Eq. (20)] requires an eigensolution in the entire semiconductor domain, which can be costly and inefficient when simulating realistic nanoscale systems.

B. Multiscale approach

Typical semiconductor nanostructures contain regions where the semiclassical models are valid, but they also contain regions where quantum effects are important. If a semiclassical model is used for the entire device, the electronic properties may not be predicted accurately in the region where quantum effects are important. On the other hand, if quantum-mechanical models are used for the entire device, the extremely high computational cost limits the size of the device that can be simulated. Multiscale models, which seamlessly combine the semiclassical and quantum models, can be accurate and efficient to predict the electronic properties of semiconductor nanostructures. The use of direct domain decomposition, where the TB, EMS, and semiclassical models are employed in different regions and combined through interface boundary conditions, can be hard to implement as the wave functions are nonlocal and imposition of a wave function as a boundary condition between the semiclassical and quantum regions can be difficult.

To overcome this difficulty, we develop a multiscale model which seamlessly combines quantum-mechanical and semiclassical models. In the region or at the Poisson grid points where the semiclassical model is not valid, the Poisson grid point is represented by heterogeneous fine-scale models or the quantum models (see Fig. 1). A Hamiltonian is first constructed by using the TB atoms or the Schrödinger grid points. Using the Hamiltonian, the elements of the Green's function (GF) matrix are then computed by[28–30]

$$\begin{aligned}\lim_{\eta\to 0^+}G_{j,j'}(E+\mathrm{i}\eta)&=\lim_{\eta\to 0^+}\{[(E+\mathrm{i}\eta)\mathbf{I}-H]^{-1}\}_{j,j'}\\&=\lim_{\eta\to 0^+}\sum_n\frac{\psi_n(\mathbf{r}_j)\psi_n^{\dagger}(\mathbf{r}'_j)}{E-E_n+\mathrm{i}\eta},\\&\quad j,j'=1,2,\ldots,N_h,\end{aligned} \tag{22}$$

where $\mathrm{i}=\sqrt{-1}$, $\mathbf{I}$ is the identity matrix, $G_{j,j'}$ denotes the jth row and j'th column entry of the Green's function matrix G, N_h is the size of the Hamiltonian, E is the energy, and $\psi_n^{\dagger}(\mathbf{r}'_j)$ is the conjugate value of $\psi_n(\mathbf{r}'_j)$. The LDOS at position $\mathbf{r}_j$, denoted by $N(\mathbf{r}_j,E)$, can be expressed as the imaginary part of the diagonal elements of the GF matrix (see, e.g., Ref. 28 for details),

$$N(\mathbf{r}_j,E)=-\pi^{-1}\lim_{\eta\to 0^+}\mathrm{Im}\,G_{j,j}(E+\mathrm{i}\eta). \tag{23}$$

The LDOS can be efficiently calculated from the Green's function by using Haydock's recursion method,[15] where the Green's function is expressed as a continued fraction based on the local EMS[39] or TB Hamiltonian.

To get the charge density in the EMS region, the EMS Hamiltonian elements for electrons and holes need to be constructed first. If the Hamiltonian of electrons is used in Eq. (22), then the LDOS $[N(\mathbf{r},E)]$ computed in Eq. (23) is that of the electrons [denoted by $N_e(\mathbf{r},E)$] and if the Hamiltonian of holes is used in Eq. (22), then the hole LDOS [denoted by $N_h(\mathbf{r},E)$] is computed. After $N_e(\mathbf{r},E)$ and $N_h(\mathbf{r},E)$ are known, the electron density $n(\mathbf{r})$ and the hole density $p(\mathbf{r})$ can be obtained by

$$n(\mathbf{r})=\int_{E_C(\mathbf{r})}^{\infty}N_e(\mathbf{r},E)f_e(E)dE, \tag{24}$$

$$p(\mathbf{r})=\int_{-\infty}^{E_V(\mathbf{r})}N_h(\mathbf{r},E)f_h(E)dE, \tag{25}$$

where $f_e(E)$ is the Fermi-Dirac distribution for electrons given by

$$f_e(E) = \frac{1}{1 + e^{(E-E_F)/k_BT}}, \tag{26}$$

and $f_h(E)$ is the Fermi-Dirac distribution for holes given by

$$f_h(E) = \frac{1}{1 + e^{(E_F-E)/k_BT}}. \tag{27}$$

Similarly, to get the charge density in the TB region, the LDOS should be first computed using the TB Green's function. The LDOS of the αth orbital at the TB atom site $\mathbf{r}_j$, denoted by $N(\mathbf{r}_j,\alpha,E)$, can also be expressed as the imaginary part of the diagonal elements of the GF matrix,

$$N_e(\mathbf{r}_j,\alpha,E) = -\pi^{-1} \lim_{\eta\to 0^+} \operatorname{Im} G_{j\alpha,j\alpha}(E + i\eta). \tag{28}$$

The corresponding atomic charge on atom j, $q(\mathbf{r}_j)$, can then be computed by

$$q(\mathbf{r}_j) = -\left[\sum_{\alpha} \int_{-\infty}^{\infty} N_e(\mathbf{r}_j,\alpha,E) f_e(E) dE - Z_c\right], \tag{29}$$

where if atom j is a silicon atom, then ionic core charge $Z_c = 4.0$, and if atom j is a hydrogen atom, then $Z_c = 1.0$.[27] Thus, the charge density $\rho(\mathbf{r})$ can be obtained by

$$\rho(\mathbf{r}) = e\left[\frac{q(\mathbf{r})}{V_{\mathrm{Si}}} + N_D^+(\mathbf{r}) - N_A^-(\mathbf{r})\right], \tag{30}$$

where V_{Si} is the effective volume occupied by a silicon crystal atom.

Comparing Eqs. (24), (25), and (30) with Eqs. (13) and (14), we note that the wave functions are not required explicitly in the LDOS approach to compute the electron and hole density. In addition, for each sampling region, we only need to compute the LDOS at the Poisson point (or the corresponding Schrödinger point or the corresponding TB atom site), where the sampling region is centered.

In summary, in the multiscale model described above, instead of directly coupling the semiclassical and quantum-mechanical regions, in the regions where semiclassical theory is not valid, the LDOS method is applied. This approach enables seamless coupling of the quantum-mechanical theory into the semiclassical theory.

1. Size of the sampling region

As shown in the last section, the size of the sampling regions directly determines the computational cost of the multiscale method. The nearsightedness principle is a useful concept that can guide the size of the sampling region. According to the nearsightedness principle,[13,14] the local electronic properties such as the local charge density only depend significantly on the effective external potential in the nearby region. The changes of that potential, no matter how large, beyond a distance R_S, have a limited effect on the local electronic properties, which rapidly decay to zero as a function of R_S.[14] Prodan and Kohn[14] gave an approximate expression for the nearsightedness radius $R(r_0,\Delta n)$ centered at r_0 for an electronic system as

$$R(r_0,\Delta n) \approx \frac{1}{2q_{\mathrm{eff}}} \ln \frac{\tilde{n}}{\Delta n}, \tag{31}$$

where q_{eff} is the decay constant of the density matrix given by $q_{\mathrm{eff}} = \frac{1}{2}\sqrt{E_g m^*/\hbar^2}$, m^* is the effective mass of electrons (holes), $\tilde{n}$ is the local density which can be approximated by the equilibrium charge density at r_0, $\rho(r_0)$, and Δn is the finite maximum asymptotic charge density due to any perturbation outside the circle of radius R. $R(r_0,\Delta n)$ defines the radius where the change in density at r_0 as a result of any perturbation outside of R does not exceed Δn. For example, from Eq. (31), if we require the relative density error to satisfy the condition $\frac{\Delta n}{\tilde{n}} < 5\times 10^{-3}$, we obtain the nearsightedness radius for silicon to be approximately 6 nm. The nearsightedness principle can guide the determination of the size of sampling regions taking the accuracy level into account. In this paper, we choose the radius of the sampling region R_S to be equal to the nearsightedness radius for simplicity.

2. Criterion for choosing tight-binding or effective-mass Schrödinger models

If the silicon crystal structure within the sampling region is not perfect, then the EMS theory is typically not valid, i.e., if there are defects, material inhomogeneities, or surface states (non-bulk-like states) within the sampling region, then the TB method is more appropriate at the sampling point. Another consideration is, for sampling regions with no inhomogeneities, as long as the TB method gives approximately the same local effective masses and band gap as the EMS method, then the EMS approach is accurate enough to compute the electronic properties in the local region. When the critical size of the silicon nanostructure is smaller than a few nanometers, the EMS approach can deviate from the TB method. Several papers have addressed this issue.[31,32] When the radius of a silicon nanocluster is larger than 2.172 nm (equivalent to 32 silicon layers within the sampling region), the deviation of the local effective mass and the band gap obtained by the TB and EMS methods is smaller than a few percent at the center region of the cluster.[31,32] These results are also consistent with the prediction from the nearsightedness principle: if we choose sampling regions with radii of 1.629 nm (24 silicon layers), 2.172 nm (32 silicon layers), and 2.716 nm (40 silicon layers), the relative density errors between the TB and EMS methods are within 15%, 7%, and 3% by using Eq. (31). These conclusions then lead to our criterion for determining an appropriate quantum-mechanical model by considering a sampling region of radius 2.716 nm. If the silicon atomic structure within the sampling region is a perfect crystal structure (that is, no dangling bonds, defects, impurities, dislocations, surfaces, etc., within the sampling region), then we can use the EMS method to compute the local electronic properties without much loss of accuracy; otherwise, the TB model is needed.

3. Criterion for choosing semiclassical or quantum-mechanical physical models

Quantum-mechanical effects diminish when the quantum confinement is negligible. In this case, semiclassical models

can be employed to increase the efficiency and avoid the complexity of quantum-mechanical methods.[16] To determine whether the local region is quantum-mechanical or semiclassical, we use the quantum potential criterion.[33–39] When the electrons are the major carriers in the device, the quantum potential $\phi_q(\mathbf{x})$ is given by

$$\phi_q(\mathbf{x}) = -\frac{\hbar^2}{8}\left\{\frac{\partial}{\partial x}\left[\frac{1}{m_x^*}\frac{\partial \ln n(\mathbf{x})}{\partial x}\right] + \frac{\partial}{\partial y}\left[\frac{1}{m_y^*}\frac{\partial \ln n(\mathbf{x})}{\partial y}\right]\right\}. \quad (32)$$

When the holes are the major carriers in the device, $n(\mathbf{x})$ is replaced by $p(\mathbf{x})$, and the electron effective masses are replaced by the hole effective masses. To determine whether the sampling Poisson point is semiclassical or quantum mechanical, we first calculate the quantum potential by Eq. (32). By comparing the quantum potential $\phi_q(\mathbf{x})$ with the coulomb potential $\phi(\mathbf{x})$, the semiclassical model is used at the sampling Poisson point if $|\phi_q(\mathbf{x})|/\max|\phi(\mathbf{x})| \leq \nu_{\text{tol}}$, where ν_{tol} is the given tolerance; otherwise, the quantum-mechanical model is used at the sampling Poisson point.

C. Dislocation theory

To demonstrate the accuracy and efficiency of the multiscale method for materials with inhomogeneities, we simulate a silicon nanostructure with 90° single period partial dislocations. The 90° partial dislocation is one of the most common types of dislocations found in silicon.[40,41] It lies along $\langle 110\rangle$ directions in $\{111\}$ slip planes and it has a Burgers vector of the type $\frac{1}{6}\langle 112\rangle$.[40,42,43] The 90° partial dislocation is assumed to have a reconstructed core,[45] and several possible reconstructions have been suggested. The two which have been shown by simulation to be stable[46–48] are the single period (SP) and double period structures. In this work, we only focus on the 90° SP partial dislocation. The 90° SP partial dislocation is believed to undergo reconstruction of their cores to eliminate unsaturated bonds and restore fourfold coordination to all atoms. In this 90° SP partial reconstruction, the displacement breaks the mirror symmetry normal to the dislocation line, enabling threefold coordinated atoms in the unreconstructed core [Fig. 3(a)] to come together and bond. This core reconstruction is shown in Fig. 3(b).

The partial dislocation is associated with shallow states above the valence band, i.e., the energy gap is reduced due to the dislocation reconstruction.[49] The reconstruction breaks the symmetry of the crystal structure. As a result, the application of the EMS method can be inaccurate, thereby necessitating the use of the TB method. For the dislocation geometry and positions of the atoms, we use the set of relaxed atomic coordinates for the 90° single period partial dislocations from Ref. 44 in our calculation.

D. Algorithm for the self-consistent multiscale model

Algorithm 1 (Table II) summarizes the procedure for the self-consistent electrostatic analysis of semiconductor nanostructures by using the combined semiclassical/EMS/TB multiscale approach.

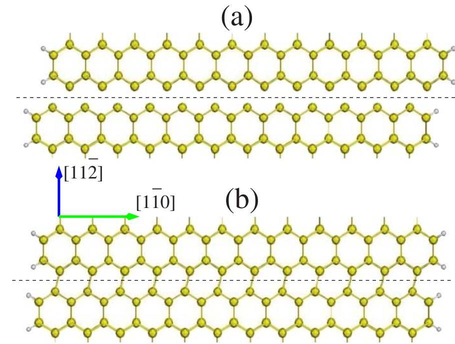

FIG. 3. (Color online) Core structure of the 90° partial dislocation looking down on the (111) slip plane. The dislocation (along the broken line) is in the $[1\bar{1}0]$ direction. (a) Unreconstructed core. (b) SP reconstruction. Note that the bonding breaks the mirror symmetry normal to $[1\bar{1}0]$ that existed in the unreconstructed core.

III. RESULTS

A. Two-dimensional fixed-fixed beam case

To illustrate the multiscale model, we first choose a 2D fixed-fixed silicon beam, as shown in Fig. 4. The x axis of the beam is chosen along the [100] direction and the beam comprises (100) faces on all sides. The p-doped (10^{20} cm^{-3}) silicon beam is clamped above a ground plane. A voltage, V_{app}, is applied between the ground plane and the beam. The silicon surface dangling bonds are terminated with hydrogen atoms. The Schottky contact effect and tunneling effect are ignored in this case for simplicity. The width W and the length L of the beam are equal to 10.864 nm. The gap G between the beam and the ground plane is set to 2.716 nm. We assume that the beam and the bottom conductor are infinitely long along the z axis (the z axis is pointing out of the paper). To compute the charge density distribution, we first discretize the domain to Poisson grid points. The Poisson grid spacings along the x axis and the y axis are denoted by Δx_P and Δy_P, respectively.

To understand how the various parameters in the multiscale model affect the accuracy, efficiency, and convergence

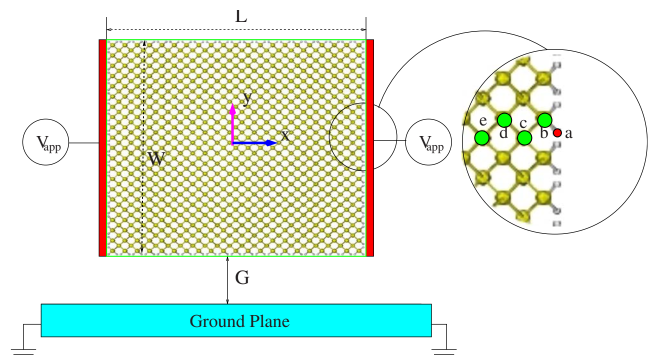

FIG. 4. (Color online) A typical nanoswitch consisting of a fixed-fixed semiconductor and a bottom conductor, where $L=W=10.864$ nm and $G=2.716$ nm with an applied voltage $V_{\text{app}}=-10.0$ V.

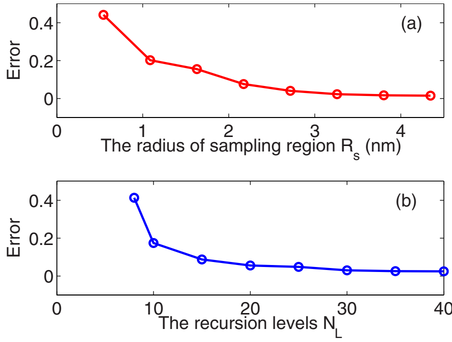

FIG. 5. (Color online) Comparison of error between the multiscale approach and the full TB model as a function of R_S and N_L. Error is defined as error$=1/(|\rho|^{ref}_{\max})\sqrt{1/N_P\Sigma_{i=1}^{N_P}[\rho^{ref}(\mathbf{x}_i)-\rho^{a}(\mathbf{x}_i)]^2}$, where ρ^{ref} and ρ^{a} are the reference full TB solution and the multiscale solution, respectively, obtained by using $\Delta x_P=\Delta y_P=0.2716$ nm. When computing the error by varying N_L in subplot (b), the sampling radius R_S is set equal to 2.716 nm.

rate of the method, we first study the impact of the sampling radius R_S on the convergence rate. The effect of the EMS sampling radius has been investigated in Ref. 39, which gave an optimized EMS sampling radius of 6 nm. Here, we only investigate the effect of the TB sampling radius. To check the convergence rate of the multiscale method, we first model the entire domain by directly solving the TB eigenproblem as a reference and denote it as the full TB method. Figure 5(a) shows the error between the multiscale method and the full TB method as a function of the TB sampling radius R_S, where R_S is varied from 0.5432 nm (equivalent to 8 layers of silicon atoms within the sampling region) to 4.3456 nm (64 layers of atoms). From Fig. 5(a), we observe that the error decays as R_S increases. When R_S is equal to 2.716 nm (equivalent to 24 layers of atoms), the error between the multiscale model and the full TB model is below 4%.

Next, we study how the recursion levels N_L influence the convergence rate for a given R_S=2.716 nm. Figure 5(b) shows the error as a function of N_L, when N_L is varied from 10 to 40 levels. From Fig. 5(b), we notice that the error decays quickly as N_L increases. When N_L is 30, the error between the multiscale model and the full TB model is less than 5%. Because a larger sampling radius and a higher number of recursion levels do not significantly improve the accuracy but demand significantly higher computational cost, we choose R_S=2.716 nm and N_L=30 in this work.

By using the quantum criteria, three kinds of regions are identified in the silicon beam, as shown in Fig. 6. The TB, EMS, and semiclassical regions are displayed by circles, + symbols, and dots, respectively. The big and small circles represent the silicon and hydrogen atoms, respectively. The outermost atoms of the silicon beam influenced by the surface states are identified as the TB region by using the TB criterion. In this case, the y component of the electric field in the middle region of the beam is so strong that the quantum confinement region is pushed deep into the beam, where the characteristic length of the quantum confinement region is larger than the characteristic length of the surface states.

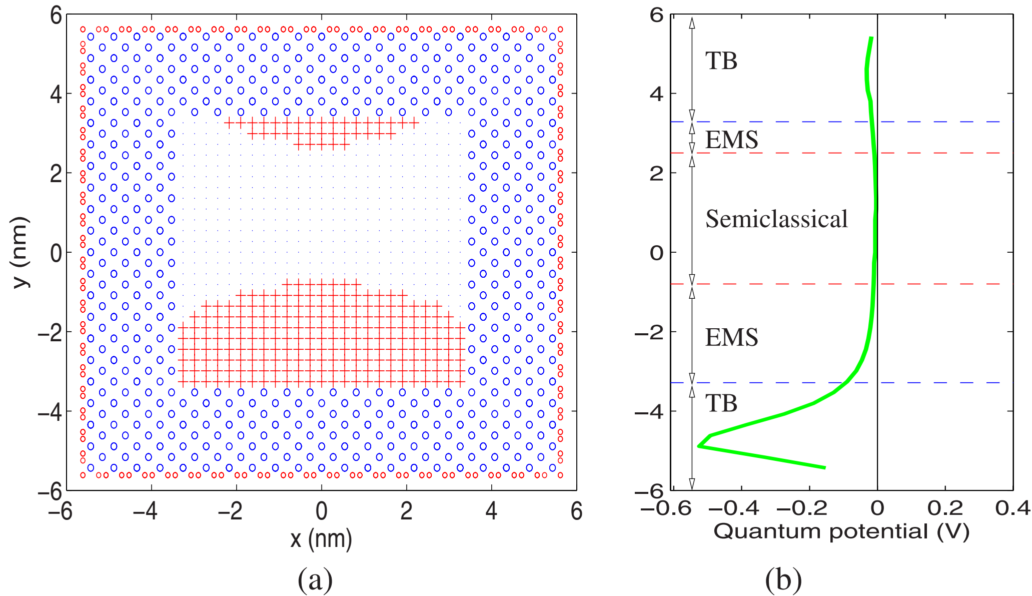

FIG. 6. (Color online) Illustration of the multiscale domain and quantum potential for the fixed-fixed silicon beam with dimensions of $L=W=10.864$ nm and $G=2.716$ nm. The semiclassical model is applicable at the sampling Poisson point if $|\phi_q(\mathbf{x})|/\max|\phi|\leq\nu_{\text{tol}}$, where ν_{tol} is the given tolerance (a value of 5×10^{-2} is used here). (a) The circles, the +, and the dots indicate the TB, EMS, and semiclassical regions, respectively. The big and small circles represent silicon and hydrogen atoms, respectively. The TB, EMS, and semiclassical regions occupy about 72%, 12%, and 16% of the beam, respectively. Plot (b) shows the quantum potential along the y axis at x=0. Because the quantum potential is almost negligible in the central region, the semiclassical model is used. In the other regions, where the quantum potential is significant, the quantum mechanical models are required. Near the surfaces, where the surface states are important, the TB method is applied; otherwise, quantum-mechanical region is identified as the EMS region.

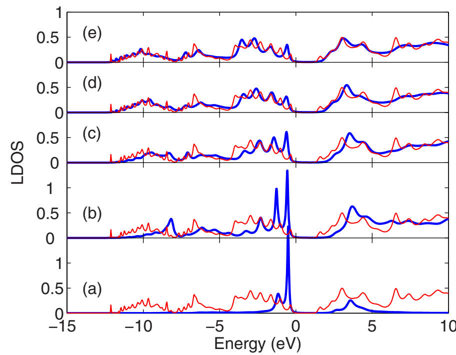

FIG. 7. (Color online) The tight-binding LDOS of various atoms near the edge of a silicon beam. The thin lines represent the LDOS of a central silicon atom in the beam. The thick lines are the LDOS of the various surface atoms shown in Fig. 4. (a) LDOS of the surface hydrogen atom *a* shown in Figs. 4. [(b)–(e)] LDOS of silicon atoms *b*–*e* shown in Fig. 4. The surface states decrease quickly as we move into the inner region from the surface.

Furthermore, the *y* component of the electric field in the middle region is much stronger compared to that at edges. As a result, two semielliptic EMS regions are identified by the quantum potential criterion, as shown in Fig. 6.

Figure 7 shows the tight-binding LDOS of five atoms (denoted as *a* to *e* in Fig. 4) at or near the surface of the silicon beam. Because the LDOS near the edges of the conduction bands and the valence bands contributes most to the charge density due to the Fermi distribution, we focus on the LDOS comparison there. Although the surface states generated by Si-H bonds are mainly located outside the energy gap,[50] they can still significantly change the LDOS near the edges of the valence and conduction bands when compared to the LDOS of silicon atoms in the interior region. The difference in the LDOS between the surface and interior states induces the nonzero partial charges. The surface states only exist for the first few surface layers and decrease quickly as we move into the interior region.

A comparison of the detailed solutions for the electron density and potential obtained by the EMS, TB, and multiscale methods is presented in Fig. 8. The potential and charge distributions along the *y* axis for $x=0$ cross section and along the *x* axis for $y=0$ cross section obtained with the EMS, TB, and multiscale models are compared in Figs. 8(a)–8(d). From these results, we find that the charge density with the EMS method close to the boundary is much different from that of the multiscale method [see Figs. 8(c) and 8(d)] because the EMS method simply ignores all the surface states. Although the nonphysical surface states are removed

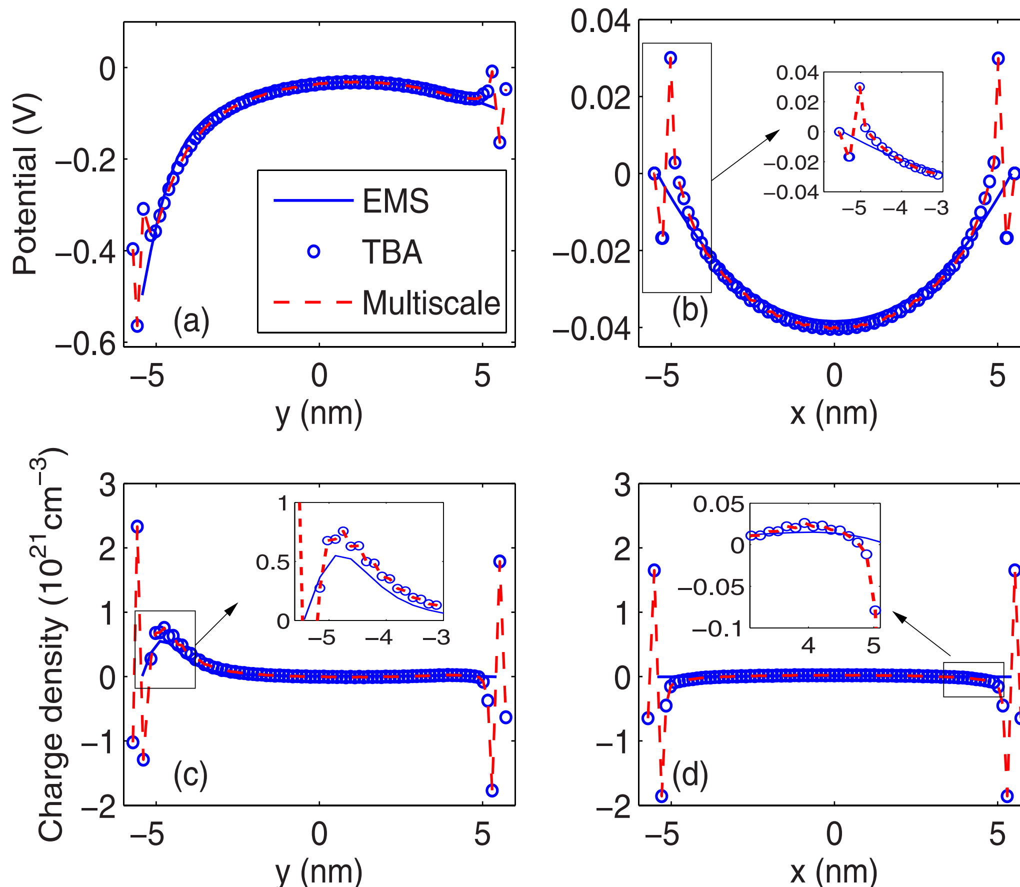

FIG. 8. (Color online) Comparison of the potential obtained from the EMS, TB, and multiscale models. Plots (a) and (b) compare the potential computed by the multiscale, EMS, and TB models along the *y* axis for $x=0$ cross section and along the *x* axis for $y=0$ cross section, respectively. Plots (c) and (d) compare the charge density computed by the multiscale, EMS, and TB models along the *y* axis for $x=0$ cross section and along the *x* axis for $y=0$ cross section, respectively.

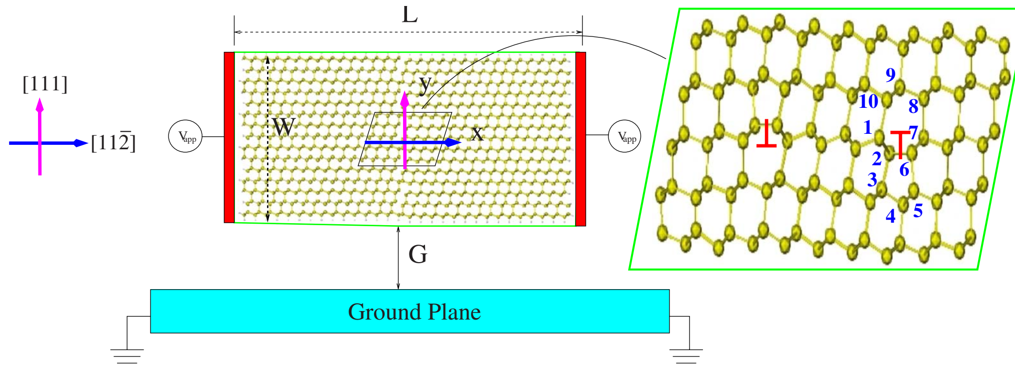

FIG. 9. (Color online) A silicon beam with two opposite 90° SP partial dislocations is clamped above a ground plane, where $L=39.9024$ nm, $W=19.7505$ nm, and $G=2.1945$ nm with an applied voltage $V_{\mathrm{app}}=-10.0$ V. The two partial dislocations located near the center of the beam have opposite Burgers vectors with a separation of 1.27 nm. The plane of the page is $(1\bar{1}0)$. The stacking fault is located between "⊥" and "⊤." The dislocation lines are perpendicular to the paper plane. The atomic coordinates of the reconstructed dislocation cores are taken from Ref. 44. Each 90° SP partial dislocation is characterized by the intersection of a fivefold and a sevenfold ring. For example, for the dislocation on the right side, the fivefold ring is composed of atoms 2-3-4-5-6-2 and the sevenfold ring contains atoms 1-2-6-7-8-9-10-1. The key feature of the relaxed geometry is that all the atoms are now truly fourfold coordinated, i.e., all four neighboring atoms are within a few percent of the ideal bond length and there is no dangling bond in the dislocation core (Ref. 44).

by terminating dangling silicon bonds with hydrogen atoms, the nonzero Mulliken partial charges at silicon surface atoms and hydrogen atoms still significantly influence the surface electronic properties. The smoothly varying EMS electron density near the boundary results in a different potential distribution compared to the multiscale method [see Figs. 8(c) and 8(d) insets], in which the electron density oscillates due to the surface partial charges. Due to the different density distribution, the potential distribution obtained from the EMS and multiscale methods is also different [see Figs. 8(a) and 8(b)]. From these results, we observe that the EMS model does not correctly predict the electronic properties near surface regions, whereas the multiscale model can reproduce the results of the full TB model. For this example, although the TB region occupies about 72% of the beam, the multiscale method is still about 40 times faster compared to directly solving the TB model.

B. Two-dimensional fixed-fixed beam with dislocations

To further explore the effectiveness of the multiscale method, we simulate a silicon beam with two 90° SP partial dislocations and study the influence of dislocations on electronic properties. The silicon structure is shown in Fig. 9. The width of the beam is denoted by W, the length is L, and the gap is G. The doping density is the same as in the first case and the Schottky contact effects and tunneling effects are also ignored in this example. The two dislocations lie near the center of the beam along $\langle 110\rangle$ separated by 1.27 nm in the (111) slip plane with opposite Burgers vectors of the type $1/6\langle 112\rangle$.

By using the criteria discussed in Sec. II B 3, three kinds of quantum regions are identified, as shown in Fig. 10. The first quantum region is formed by the surface states which surround the entire nanostructure. The second kind (the two EMS regions denoted by + in Fig. 10) is the quantum confinement region formed by the applied electric field where the electrons are confined and the energy levels are quantized. The third quantum region is formed by the dislocations where the stacking fault is located and the EMS approach is not accurate. The TB quantum region is about 41% of the entire domain in this case.

The LDOSs of several silicon atoms near the dislocation core (see Fig. 9 for the location of the atoms) are plotted in Fig. 11. The thin lines represent the LDOS of a reference silicon atom far from the dislocation and the surface. The thick lines represent the LDOS of the representative atoms (denoted by 1–10 in Fig. 9) near the dislocation core. From the figure, the dislocation induces a shallow state above the

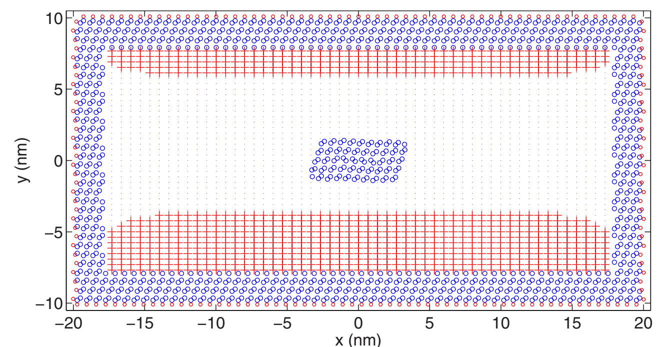

FIG. 10. (Color online) Illustration of the multiscale domain for the fixed-fixed silicon beam with dimensions of $L=39.9024$ nm, $W=19.7505$ nm, and $G=2.1945$ nm. The Poisson grid spacings are $\Delta x_P=0.6650$ nm and $\Delta y_P=0.3135$ nm. The semiclassical model is applicable at the sampling Poisson point if $|\phi_q(\mathbf{x})|/\max|\phi|\leq\nu_{\mathrm{tol}}$, where ν_{tol} is the given tolerance (a value of 5×10^{-2} is used here). The circles, the +, and the dots indicate the TB, EMS, and semiclassical regions, respectively. The big and small circles represent silicon and hydrogen atoms, respectively. The TB, EMS, and semiclassical regions occupy about 41%, 16%, and 43% of the beam, respectively.

TABLE II. A complete algorithm for self-consistent multiscale electrostatic analysis of semiconductor nanostructures.

Algorithm 1

1: Discretize the domain of the semiconductor beam into N_P Poisson grid points for solving the Poisson equation and discretize the boundary of the domain (if any) into grid points for solving boundary integral equation (BIE).[39]

2: Set k=0, solve the semiclassical Poisson model and obtain the initial potential distribution $\phi^{(0)}$, electron density $n^{(0)}$, and hole density $p^{(0)}$.

3: **repeat**

4: **for** each Poisson grid point, i=1 to N_P **do**

5: use the criteria to choose the appropriate physical model at the Poisson grid point

6: **if** the physical model is TB **then**

7: define the local sampling region by Eq. (31) according to the desired accuracy level and construct the entries of the local TB Hamiltonian matrix using $\phi^{(k)}$. Compute the LDOS and $\rho_i^{(k+1)}$ at the TB atom site ($\mathbf{r}_j$=$\mathbf{x}_i$) using Eqs. (28-30)

8: **else if** the physical model is EMS **then**

9: define the local sampling region by Eq. (31), discretize the sampling region into Schrödinger grid points, construct the entries of the local EMS Hamiltonian matrix by using $\phi^{(k)}$, and compute the LDOS and $n_i^{(k+1)}$ and $p_i^{(k+1)}$ at the Schrödinger point ($\mathbf{r}_j$=$\mathbf{x}_i$) using Eqs. (24-25)

10: **else if** the physical model is $semiclassical$ **then**

11: compute the charge density $n_i^{(k+1)}$ and $p_i^{(k+1)}$ using Eq. (9) and Eq. (10)

12: **end if**

13: **end for**

14: solve the coupled BIE/Poisson equations to update the potential distribution $\phi^{(k+1)}$

15: $k=k+1$

16: **until** a self-consistent solution is obtained when $\max|n_i^{(k)}-n_i^{(k-1)}|<\theta^{\rho}_{\text{tol}}$, $\max|p_i^{(k)}-p_i^{(k-1)}|<\theta^{\rho}_{\text{tol}}$ and $\max|\phi_i^{(k)}-\phi_i^{(k-1)}|<\theta^{\phi}_{\text{tol}}$, where $\theta^{\rho}_{\text{tol}}$ and $\theta^{\phi}_{\text{tol}}$ are the error tolerances for the charge density and potential, respectively.

17: Output the results.

valence band and reduces the energy gap. The dislocation core results in nonzero partial charges along the dislocation line. The dislocation effects decay quickly when the atoms are far away from the core. The dislocation reconstruction due to stacking fault breaks the symmetry of the crystal structure, thus making it necessary to use the TB method.

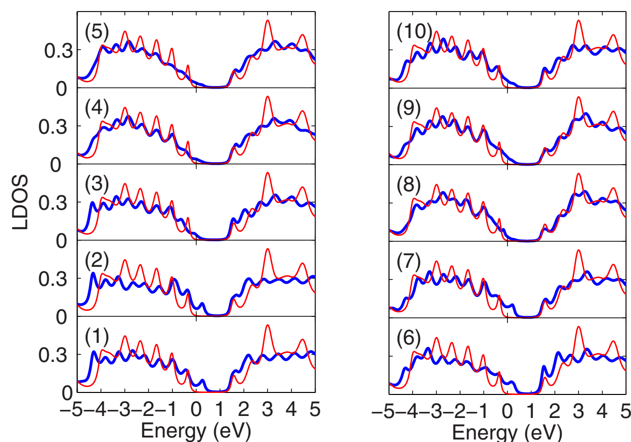

FIG. 11. (Color online) The LDOS of ten silicon atoms (denoted in Fig. 9) near the dislocation core. The thick and thin lines represent the LDOS of the atoms near the dislocation core and for an interior silicon atom far from the dislocation in the beam, respectively. [(1)–(10)] LDOS of atoms 1–10 (see Fig. 9) which surround the dislocation core. The influence of the dislocation states decreases quickly when the atoms are far away from the dislocation core.

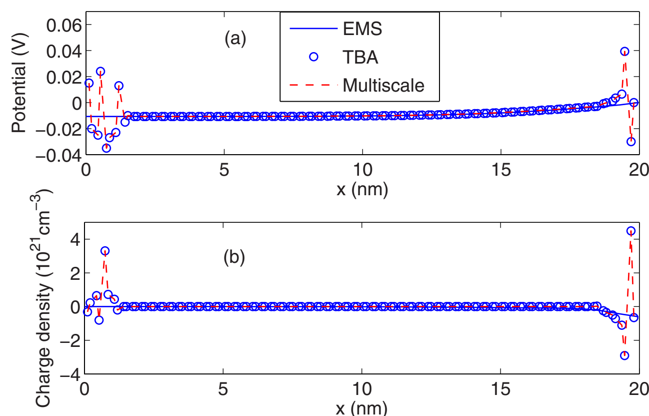

FIG. 12. (Color online) Comparison of the potential and charge density obtained from the multiscale, EMS, and TB models. Plots (a) and (b) compare the potential and charge distribution computed by the multiscale, EMS, and TB models along the positive x axis ($x \geqslant 0$) for $y=0$ cross section.

Since the conduction band energy and electron density near the dislocation core are the interesting features, we focus on the distribution along the positive x axis for $y=0$ cross section obtained by the EMS, TB, and multiscale models (see Fig. 12). The charge density deviation between the multiscale and EMS models indicates that the EMS approach is not accurate near the dislocation and surface regions and the TB model is needed. The multiscale method is about 8 times slower compared to the full EMS method but over 600 times faster than the full TB method. The additional cost of the multiscale method compared to the EMS method is due to the fact that the TB quantum region occupies 41% of the beam. From these results, we can conclude that the multiscale method is an accurate and efficient tool to compute the electronic properties of silicon nanostructures.

IV. CONCLUSIONS

A heterogeneous multiscale model combining semiclassical, effective-mass Schrödinger, and tight-binding approaches has been presented in this paper for the electrostatic analysis of silicon nanoelectromechanical systems. Quantum criteria are used to identify semiclassical, EMS, and TB regions. In the regions where quantum effects are significant, the charge densities are computed by considering sampling regions and the LDOS. The LDOS is efficiently calculated by using Haydock's recursion method. The multiscale method has been shown to be accurate by comparing with the full TB method. When the TB regions are significant, the multiscale method has been shown to be several orders of magnitude faster compared to the direct solution of the full TB method. When the quantum regions are small, the multiscale method approaches the efficiency of the semiclassical method. By considering examples of silicon NEMS with hydrogen surface termination and 90° SP partial dislocations, we have also shown that the multiscale method efficiently and seamlessly coupled the different physical models into one framework without loss of accuracy.

ACKNOWLEDGMENTS

This work is supported by the National Science Foundation under Grant Nos. 0228390 and 0601479, by DARPA/MTO, and by SRC.

*Corresponding author: aluru@uiuc.edu; http://www.uiuc.edu/~aluru

[1] J. Q. Broughton, F. F. Abraham, N. Bernstein, and E. Kaxiras, Phys. Rev. B **60**, 2391 (1999).
[2] W. E and B. Engquist, Commun. Math. Sci. **1**, 87 (2003).
[3] W. Cai, M. de Koning, V. V. Bulatov, and S. Yip, Phys. Rev. Lett. **85**, 3213 (2000).
[4] T. Shimokawa, J. J. Mortensen, J. Schiotz, and K. W. Jacobsen, Phys. Rev. B **69**, 214104 (2004).
[5] G. Lu, E. B. Tadmor, and E. Kaxiras, Phys. Rev. B **73**, 024108 (2006).
[6] Z. Tang, H. Zhao, G. Li, and N. R. Aluru, Phys. Rev. B **74**, 064110 (2006).
[7] W. E, B. Engquist, and Z. Huang, Phys. Rev. B **67**, 092101 (2003).
[8] R. F. Pierret, *Semiconductor Device Fundamentals* (Addison-Wesley, Reading, MA, 1996).
[9] G. Li and N. R. Aluru, J. Appl. Phys. **96**, 2221 (2004).
[10] J. H. Kane, *Boundary Element Analysis in Engineering Continuum Mechanics* (Prentice-Hall, Englewood Cliffs, NJ, 1994).
[11] J. D. Jackson, *Classical Electrodynamics*, 3rd ed. (Wiley, New York, 1999).
[12] G. E. Forsythe and W. R. Wasow, *Finite-Difference Methods for Partial Differential Equations* (Wiley, New York, 1960).

[13] W. Kohn, Phys. Rev. Lett. **76**, 3168 (1996).
[14] E. Prodan and W. Kohn, Proc. Natl. Acad. Sci. U.S.A. **102**, 11635 (2005).
[15] R. Haydock, *Recursion Method and Its Applications* (Springer-Verlag, Berlin, 1985).
[16] K. Hess, *Advanced Theory of Semiconductor Devices* (Prentice-Hall, Englewood Cliffs, NJ, 1988).
[17] Z. Tang, Y. Xu, G. Li, and N. R. Aluru, J. Appl. Phys. **97**, 114304 (2005).
[18] T. B. Boykin, G. Klimeck, and F. Oyafuso, Phys. Rev. B **69**, 115201 (2004).
[19] J. C. Slater and G. F. Koster, Phys. Rev. **94**, 1498 (1954).
[20] P. Vogl, H. P. Hjalmarson, and J. D. Dow, J. Phys. Chem. Solids **44**, 365 (1983).
[21] W. A. Harrison, *Elementary Electronic Structure*, revised ed. (World Scientific, Singapore, 2004).
[22] W. A. Harrison, Phys. Rev. A **7**, 1876 (1973).
[23] W. A. Harrison, Phys. Rev. B **27**, 3592 (1983).
[24] W. A. Harrison, Phys. Rev. B **31**, 2121 (1985).
[25] Y. Zheng, C. Rivas, R. Lake, K. Alam, T. B. Boykin, and G. Klimeck, IEEE Trans. Electron Devices **52**, 1097 (2005).
[26] A. P. Sutton, *Electronic Structure of Materials* (Clarendon, Oxford, 1994).
[27] J. A. Majewski and P. Vogl, Phys. Rev. B **35**, 9666 (1987).
[28] E. N. Economou, *Green's Functions in Quantum Physics* (Springer-Verlag, Berlin, 1983).
[29] C. Lanczos, J. Res. Natl. Bur. Stand. **45**, 255 (1950).
[30] A. Jennings and J. J. McKeown, *Matrix Computation* (Wiley, New York, 1992).
[31] J. Wang, A. Rahman, A. Ghosh, G. Klimeck, and M. Lundstrom, IEEE Trans. Electron Devices **52**, 1589 (2005).
[32] J. Sée, P. Dollfus, and S. Galdin, Phys. Rev. B **66**, 193307 (2002).
[33] D. K. Ferry, S. Ramey, L. Shifren, and R. Akis, J. Comput. Electron. **1**, 59 (2002).
[34] D. K. Ferry, Superlattices Microstruct. **27**, 61 (2000).
[35] H. L. Grubin, J. P. Kreskovsky, T. R. Govindan, and D. K. Ferry, Semicond. Sci. Technol. **9**, 855 (1994).
[36] I. Knezevic, D. Vasileska, and D. K. Ferry, IEEE Trans. Electron Devices **49**, 1019 (2002).
[37] A. Asenov, J. R. Watling, A. R. Brown, and D. K. Ferry, J. Comput. Electron. **1**, 503 (2002).
[38] S. S. Ahmed, C. Ringhofer, and D. Vasileska, IEEE Trans. Nanotechnol. **4**, 465 (2005).
[39] Y. Xu and N. R. Aluru, Phys. Rev. B **76**, 075304 (2007).
[40] J. P. Hirth and J. Lothe, *Theory of Dislocations* (McGraw-Hill, New York, 1982).
[41] F. R. N. Nabarro, *Dislocations in Solids* (North-Holland, Amsterdam, 1989).
[42] S. Marklund, Phys. Status Solidi B **92**, 83 (1979).
[43] S. Marklund, Phys. Status Solidi B **100**, 77 (1980).
[44] J. R. Chelikowsky and J. C. H. Spence, Phys. Rev. B **30**, 694 (1984).
[45] P. B. Hirsch, Mater. Sci. Technol. **1**, 666 (1985).
[46] J. R. K. Bigger, D. A. McInnes, A. P. Sutton, M. C. Payne, I. Stich, R. D. King-Smith, D. M. Bird, and L. J. Clarke, Phys. Rev. Lett. **69**, 2224 (1992).
[47] J. Bennetto, R. W. Nunes, and D. Vanderbilt, Phys. Rev. Lett. **79**, 245 (1997).
[48] A. Valladares and A. P. Sutton, J. Phys.: Condens. Matter **17**, 7547 (2005).
[49] A. Valladares and A. P. Sutton, Prog. Mater. Sci. **52**, 421 (2007).
[50] C. G. Van de Walle, Y. Bar-Yam, and S. T. Pantelides, Phys. Rev. Lett. **60**, 2761 (1988).